ADVANCED FUNCTIONAL MATERIALS
www.afm-journal.de

# Oxidized mRNA Lipid Nanoparticles for In Situ Chimeric Antigen Receptor Monocyte Engineering

*Alvin J. Mukalel, Alex G. Hamilton, Margaret M. Billingsley, Jacqueline Li, Ajay S. Thatte, Xuexiang Han, Hannah C. Safford, Marshall S. Padilla, Tyler Papp, Hamideh Parhiz, Drew Weissman, and Michael J. Mitchell**

**Chimeric antigen receptor (CAR) monocyte and macrophage therapies are promising solid tumor immunotherapies that can overcome the challenges facing conventional CAR T cell therapy. mRNA lipid nanoparticles (mRNA-LNPs) offer a viable platform for in situ engineering of CAR monocytes with transient and tunable CAR expression to reduce off-tumor toxicity and streamline cell manufacturing. However, identifying LNPs with monocyte tropism and intracellular delivery potency is difficult using traditional screening techniques. Here, ionizable lipid design and high-throughput in vivo screening are utilized to identify a new class of oxidized LNPs with innate tropism and mRNA delivery to monocytes. A library of oxidized (oLNPs) and unoxidized LNPs (uLNPs) is synthesized to evaluate mRNA delivery to immune cells. oLNPs demonstrate notable differences in morphology, ionization energy, and p$K_a$, thereby enhancing delivery to human macrophages, but not T cells. Subsequently, in vivo library screening with DNA barcodes identifies an oLNP formulation, C14-O2, with innate tropism to monocytes. In a proof-of-concept study, the C14-O2 LNP is used to engineer functional CD19-CAR monocytes in situ for robust B cell aplasia (45%) in healthy mice. This work highlights the utility of oxidized LNPs as a promising platform for engineering CAR macrophages/monocytes for solid tumor CAR monocyte therapy.**

## 1. Introduction

Immunotherapy has transformed the landscape of cancer therapeutics by utilizing exogenous signals to stimulate a dormant immune system to fight cancer, enabling improved clinical outcomes compared to conventional chemotherapeutics. Specifically of interest, chimeric antigen receptor (CAR) T cells, patient-derived autologous T cells that are virally engineered ex vivo, have had remarkable success in treating hematological cancers, generating robust and long-lasting responses in the clinic.[1–4] As of 2023, there are six Food and Drug Administration (FDA)-approved CAR T cell therapies, four targeted toward CD19 B cell cancers and two B-cell maturation antigen (BCMA)-targeted therapies to treat multiple myeloma.[5] Although these therapies have demonstrated efficacy in treating hematological cancers, they still face several challenges toward their broader application, both in terms of efficacy against other types of cancer—such as solid tumors—and

A. J. Mukalel, A. G. Hamilton, M. M. Billingsley, J. Li, A. S. Thatte, X. Han, H. C. Safford, M. S. Padilla, M. J. Mitchell
Department of Bioengineering
University of Pennsylvania
Philadelphia, PA 19104, USA
E-mail: mjmitch@seas.upenn.edu

T. Papp, H. Parhiz, D. Weissman
Department of Medicine
University of Pennsylvania
Philadelphia, PA 19104, USA

H. Parhiz, D. Weissman, M. J. Mitchell
Abramson Cancer Center
Perelman School of Medicine
University of Pennsylvania
Philadelphia, PA 19104, USA

M. J. Mitchell
Institute for Immunology
Perelman School of Medicine
University of Pennsylvania
Philadelphia, PA 19104, USA

M. J. Mitchell
Cardiovascular Institute
Perelman School of Medicine
University of Pennsylvania
Philadelphia, PA 19104, USA

M. J. Mitchell
Institute for Regenerative Medicine
Perelman School of Medicine
University of Pennsylvania
Philadelphia, PA 19104, USA

M. J. Mitchell
Penn Institute for RNA Innovation
Perelman School of Medicine
University of Pennsylvania
Philadelphia, PA 19104, USA

The ORCID identification number(s) for the author(s) of this article can be found under https://doi.org/10.1002/adfm.202312038

DOI: 10.1002/adfm.202312038

 

patient accessibility. Solid tumors present several physical and chemical barriers to CAR T cell therapy. Tumors are highly fibrotic, contain dense immunosuppressive cytokine gradients, and compete for metabolic substrates, which severely diminishes the efficacy of CAR T therapy through mechanisms of physical exclusion and inactivation of the engineered T cells.[6–9] Simultaneously, the relatively low number of patients who qualify for CAR T cell therapies is further reduced by the intricate manufacturing requirements of this treatment. In CAR T cell therapy, a patient's own T cells are isolated from peripheral blood, expanded ex vivo, and virally transduced to express a CAR before being reinfused back into the patient.[10] Only a few institutions can support the personalized nature of CAR T cell therapy, as it requires highly specialized processes, equipment, and training that are time, labor, and cost-intensive.[10–12] Together, these challenges necessitate the exploration of new engineering approaches for the development and generation of CAR-based therapies to improve their clinical impact.

Innate immune cells, such as macrophages and their circulating precursors, monocytes, have had long-standing interest as therapeutic targets for cancer immunotherapies, as these cells can account for up to 50% of the tumor mass.[13–15] Tumors secrete high levels of chemokine ligand 2 (CCL2) and colony-stimulating factor (CSF), actively recruiting circulating monocytes and promoting their extravasation from the blood and migration into the tumor.[16–18] Within the tumor, these monocytes differentiate into tumor-associated macrophages (TAMs) or myeloid-derived suppressor cells (MDSCs) which heavily contribute to the immunosuppressive tumor microenvironment.[19,20] Clinically, therapeutic approaches to combat these tumor monocytes attempt to either (1) directly block monocyte recruitment into tumors by inhibiting chemotactic signals or (2) broadly deplete monocyte populations to reduce intratumoral immunosuppressive signaling, both with varying degrees of success.[16,18,21]

In the healthy body, monocytes and macrophages carry out diverse immune functions including cytokine and chemokine secretion, phagocytosis, and antigen presentation to engage the active arm of the immune system. By integrating effector and regulatory functions, monocytes and macrophages are capable of generating a multifaceted immune response. Breakthroughs in immunoengineering, such as CAR T cell therapy, have recontextualized monocytes as a therapeutic target whose innate tumor infiltrating properties and immunoregulatory functions can be leveraged for solid tumor therapies. Prior works have engineered monocytes to ameliorate immunosuppression through the secretion of inflammatory cytokines such as interferon (IFN)-$\alpha$ and interleukin (IL)-12; however, more recent strategies engineered monocytes to express HER2-targeted CAR, allowing monocytes to directly kill tumor cells in vitro and in vivo in an antigen-specific manner.[22–26] Although this therapy route is nascent and under preclinical development, it highlights the opportunity for CAR monocytes as a new therapeutic modality to treat solid tumor malignancies.

However, conventional viral engineering of CAR T cells and next-generation targets such as CAR monocytes continue to face significant safety and technical hurdles to successful clinical translation. Viral engineering platforms such as lentiviruses and adeno-associated viruses (AAVs) can possibly integrate into the host genome and give rise to harmful mutations which, at clinically relevant scales, pose a risk to patient safety.[27–29] Further, administration of viral vectors in vivo is challenging, as vectors can interact with the immune system, eliciting systemic responses that require additional therapeutic interventions and simultaneously reduce the expression of the transgene, especially true for patients receiving multiple doses.[30–32] Perhaps most importantly, virally engineered cells express the transduced protein for extended periods of time, in some cases permanently.[29,33–37] Indeed, patients who have received virally engineered BCMA-CAR T cells suffer from expected, but lasting, loss of healthy BCMA$^+$ humoral immune cells.[38] Alternatives to viral platforms, specifically those that provide temporal control over CAR expression and can be administered safely in vivo with minimal immunogenicity, are critical for CAR therapy to realize its full potential.

mRNA-lipid nanoparticles (mRNA-LNPs) are a clinically approved non-viral delivery vector capable of generating therapeutically relevant patient responses, as evidenced by the Food and Drug Administration (FDA) approval of COVID-19 mRNA-LNP vaccines developed by Moderna and Pfizer.[39,40] mRNA-LNPs offer several advantages over viral platforms, namely in transient mRNA expression and the lower immunogenicity of LNPs compared to AAVs.[41,42] Together, these features can improve the safety and efficacy profiles for CAR therapies, especially in treating solid tumors.[43,44] Previous works have demonstrated the ability of mRNA-LNPs to facilitate CAR therapies in T cells and macrophages, in applications spanning from cancer immunotherapy to cardiac injury.[45–47] However, most of this work for cancer applications was accomplished using in vitro or ex vivo methods and the only in vivo demonstration of this technology utilized LNPs functionalized with CD5-targeted antibodies to deliver CAR mRNA to T cells for cardiac repair.[46,47] The addition of biologics such as antibodies to LNPs increases the compositional and manufacturing complexity of these technologies, adding another challenge to the regulatory process.[48] Non-targeted LNP approaches have been explored by other groups for mRNA-LNP delivery to myeloid cells such as tissue-resident macrophages in the lungs, liver, and spleen.[49] However, there have been relatively few non-viral engineering strategies developed for monocytes, let alone approaches to directly engineer these cells in situ, as they are an emerging therapeutic target.[15,17,50] Notably, of the nanoparticles developed for monocyte modulation, many platforms are lipidic, and further leverage enhanced monocyte affinity for naturally occurring oxidized lipids and oxidized lipoproteins found in circulation.[50–56] Thus, a facile approach would integrate these motifs into the design of the LNPs to engineer endogenous tropism to monocytes and circumvent the use of additional targeting moieties. However, identification of LNPs with endogenous tropism to specific tissues and cell types using conventional fluorescence-based reporter assays is low-throughput and cost-intensive, and it is well established that in vitro screening results are minimally predictive of in vivo efficacy.[57] To address this, molecular barcoding has been applied to simultaneously screen dozens of nanoparticles in vivo for cell and tissue specificity.[58–61] Typically, this is accomplished using short single-stranded DNA oligomers, where each distinct LNP formulation is used to encapsulate a unique DNA barcode and accumulation of the barcode is informative of LNP tropism to that cell or tissue type. Thus, exploring oxidized ionizable lipid nanoparticle

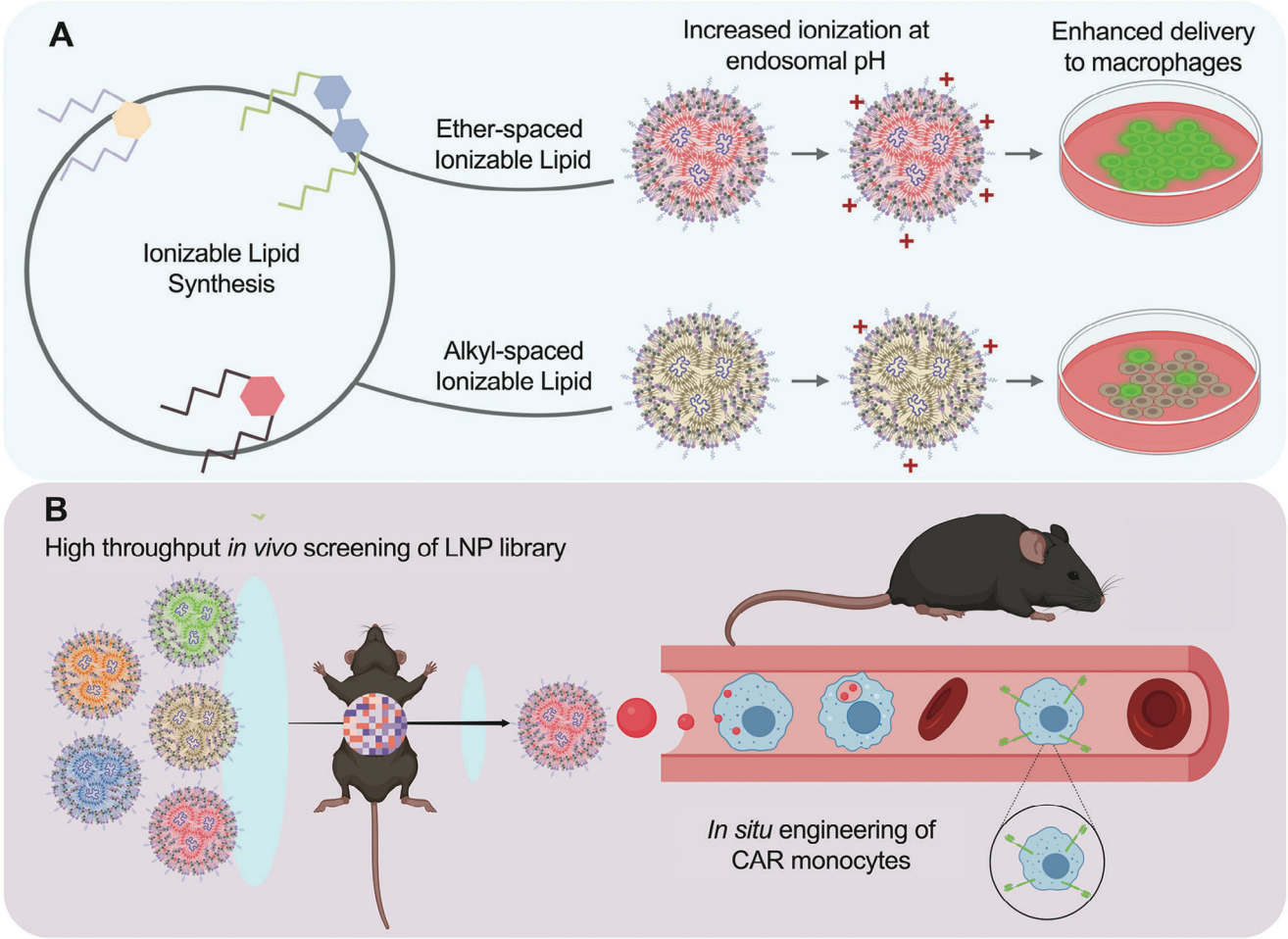


**Figure 1.** Oxidized mRNA lipid nanoparticles for in situ CAR monocyte engineering. A) Ionizable lipid design and screening were used to identify oxidized ionizable lipids, with an internal ether chemical motif, that enhanced mRNA delivery to macrophages. B) High throughput in vivo screening via DNA barcoding combined with mRNA validation studies was used to identify mRNA LNPs capable of engineering CAR monocytes directly in situ for solid tumor immunotherapy.

structures using discovery platforms such as DNA barcoding is a compelling strategy to develop mRNA-LNPs for engineering monocytes in situ.

Here, we combined lipid design, high throughput LNP screening, and mRNA-based CAR therapy to identify an LNP formulation with an innate tropism that can be used to engineer functional CAR monocytes in vivo. Taking inspiration from myeloid affinity for oxidized lipids, we designed a library of ionizable lipid structures of varying degrees of oxidation (O1, O2, and O3) and a corresponding set of unoxidized ionizable lipids (U1, U2, and U3) and formulated these ionizable lipids into oxidized lipid nanoparticles (oLNPs) or unoxidized lipid nanoparticles (uLNPs), respectively. We utilized this lipid library to understand the effect of oxidation on mRNA-LNP physicochemical properties and delivery to immune cells in vitro and in vivo. We found that oLNPs had favorable ionization and morphological properties which translated to enhanced mRNA delivery to macrophages in vitro compared to uLNPs. We employed DNA barcoding to identify LNPs with tropism to macrophages, monocytes, T cells, and B cells in vivo and confirmed functional mRNA delivery to these cells in vivo using a fluorescence-based reporter mRNA. Lastly, we demonstrated that an oLNP with high delivery to blood monocytes, C14-O2, could generate functional CD19-targeted CAR monocytes following a single intravenous administration at a dose of 1 mg $kg^{-1}$ which was confirmed through a 45% reduction in blood resident CD19+ B cells in healthy mice (B cell aplasia). This work highlights a platform for in situ CAR monocyte engineering while elucidating structural features of ionizable lipids that can be beneficial for in vitro or ex vivo engineering of human myeloid cells (**Figure 1**).

## 2. Results and Discussion

### 2.1. Synthesis and Characterization of Oxidized and Unoxidized Ionizable Lipid Nanoparticles

In previous works, it was found that LNPs containing ionizable lipids derived from a parent C12-200 molecule could potently engineer human T cells both in vitro and ex vivo.[47] These lipids varied in structure by altering the number of piperazine groups

and by introducing branched architecture or oxidation via the incorporation of additional internal oxygen atoms. Notably, the top ionizable lipids identified in those screens were all oxidized, albeit to different degrees, containing 1, 2, or 3 oxygen atoms. Thus, we were motivated to elucidate the importance of these oxidized lipids to the bioactivity of the LNPs. Further, since macrophages and monocytes play a significant homeostatic role in scavenging oxidized lipids and lipoproteins in the blood, we hypothesized that oLNPs would be well-suited for engineering these cell types. To explore this hypothesis, we synthesized a complementary set of ionizable lipids using polyamine cores that were unoxidized, where the total number of carbons in the molecule was kept constant between each pair of oxidized and unoxidized lipids (**Figure 2A**). This second-generation ionizable lipid library was synthesized using an $S_N2$ reaction between the polyamine core and epoxide-terminated alkyl tails varying in 12, 14, or 16 carbons in length (Figure 2A–C). The resultant ionizable lipids were combined into a single ethanol phase containing the excipients 1,2-dioleoyl-snglycerphosphoethanolamine (DOPE), cholesterol, and 1,2-dimyristoyl-sn-glycero-3-phosphoethanolamine-N-[methoxy(polyethylene glycol)-2000] (C14-PEG2000) and mixed with an aqueous phase containing luciferase mRNA via a microfluidic device to form LNPs. The unoxidized LNPs (uLNPs) and the oLNPs were characterized for size, zeta potential, and mRNA encapsulation (Figure S2, Supporting Information). There were minimal differences found between the oLNPs and uLNPs in terms of hydrodynamic diameter and mRNA encapsulation efficiency (Figure S2A,C, Supporting Information). Interestingly, LNPs with the highest degree of oxidation (O3) tended to have a more positive surface charge compared to their U3 counterparts at all epoxide-tail lengths (Figure S2B, Supporting Information). The differences in zeta potential suggest a relationship between the degree of oxidation and the overall protonation state, in turn affecting the net charge of the LNP at pH 7.4, where greater oxidation increased the protonation state of the LNP.

To further characterize the oLNP/uLNP library, ionization properties such as $pK_a$ and ionization energy were quantified using a 6-(p-Toluidino)-2-naphthalenesulfonic acid (TNS)-based fluorescence assay as previously described.[47,62] In general, oLNPs were found to have higher apparent $pK_a$ compared to their uLNP counterparts, with the notable exception of the O3 LNP (Figure 2D). This coincided with an increase in ionization energy, which has been demonstrated to impact LNP-mediated mRNA delivery, though this result was not seen here in the C16 lipids (Figure 2E).[62] Although TNS is used to characterize bulk LNP properties such as ionization energy and $pK_a$, the bulk signal is an aggregate of interactions between the TNS probe and microenvironments within the LNP. Thus, the observed increase in $pK_a$ could result from positive charges that are better stabilized by hydrophilic ether groups, compared to the hydrophobic alkyl groups, which is supported by the predicted differences in pH-dependent hydrophobicity (log *D*) between equivalent oxidized and unoxidized ionizable lipids (Figure S3, Supporting Information). Cryogenic transmission electron microscopy (cryo-TEM) was used to further characterize LNP morphological properties; oLNPs demonstrated spherical multilamellar morphology, consistent with that of other gold standard LNPs such as C12-200, while uLNPs were found to have less spherical and segmented morphology in comparison (Figure 2F). Empty LNPs were found within each sample, consistent with recent studies on mRNA distribution within LNP suspensions.[63] The role of LNP morphology, as determined by TEM imaging of vitrified LNPs, in LNP bioactivity is still not fully understood, as morphology emerges from a convolution of other variables such as lipid identity and LNP composition. Irregular and non-uniform LNP structures can, in some contexts, promote bioactivity, and recent work has shown that LNP polymorphism can enhance delivery via downstream effects on LNP trafficking within cells.[64–66] For phagocytic cells such as macrophages, monocytes, and dendritic cells, particle shape and size can determine the mechanisms by which particles interact and are endocytosed by cells, and can even dictate systemic immune responses.[67–70] These notable differences in LNP characteristics such as charge, ionization, and morphology provided promise that there might be subsequent differences in LNP bioactivity.

### 2.2. In Vitro Screening of oLNPs and uLNPs in Human Immune Cells

The oLNP and uLNP library was screened in phorbol 12-myristate 13-acetate (PMA)-differentiated THP-1 macrophages to compare the effect of oxidation state on LNP bioactivity in macrophages. Generally, oLNPs outperformed their uLNP counterparts at all tail lengths tested (**Figure 3A**). C12 LNPs were generally less bioactive than their C14 and C16 counterparts and, at longer tail lengths, oLNPs significantly outperformed uLNPs, with minimal toxicity (Figure 3A). The library was further screened in Jurkat T cells to ascertain if trends found in macrophages were more broadly applicable to other immune cell types. Interestingly, there was no trend between luminescence signal and epoxide tail length or oxidation state in Jurkat cells (Figure 3B) although the oLNP C14-O1 was notably superior to the rest of the library for mRNA delivery to Jurkat cells. Lastly, the library was screened in primary human macrophages derived from $CD14^+$ monocytes isolated from human peripheral blood. We identified the same trend in mRNA delivery to primary macrophages compared to THP-1 cells where oLNPs significantly outperformed uLNPs (Figure 3C).

Interestingly, there was an apparent relationship between the degree of oxidation and bioactivity in macrophages, as O2 LNPs had higher delivery compared to O1 and O3 LNPs, suggesting a local optimum for delivery that can potentially help to inform the design of future lipids for ex vivo engineering of macrophage cell therapies. The inclusion of oxidation in the form of ether groups potentially has two effects. First, ionization energy has recently been proposed as a contributing physicochemical property impacting LNP payload delivery, as protonation of the ionizable lipid is one of the proposed mechanisms of endosomal escape of LNPs and cytosolic delivery of their cargo.[62,71] For highly endocytic and phagocytic cells such as macrophages, the ability to escape acidic subcellular compartments is especially important for intracellular delivery, which could be enhanced by increased ionization and a $pK_a$ closer to early endosomal pH. For less endocytically active cells such as T cells, ionization energy may be less of a determinant for successful delivery but may instead impact biocompatibility, as uLNP-treated T cells had higher cell viability compared to oLNPs, although only one LNP, C12-O2, fell

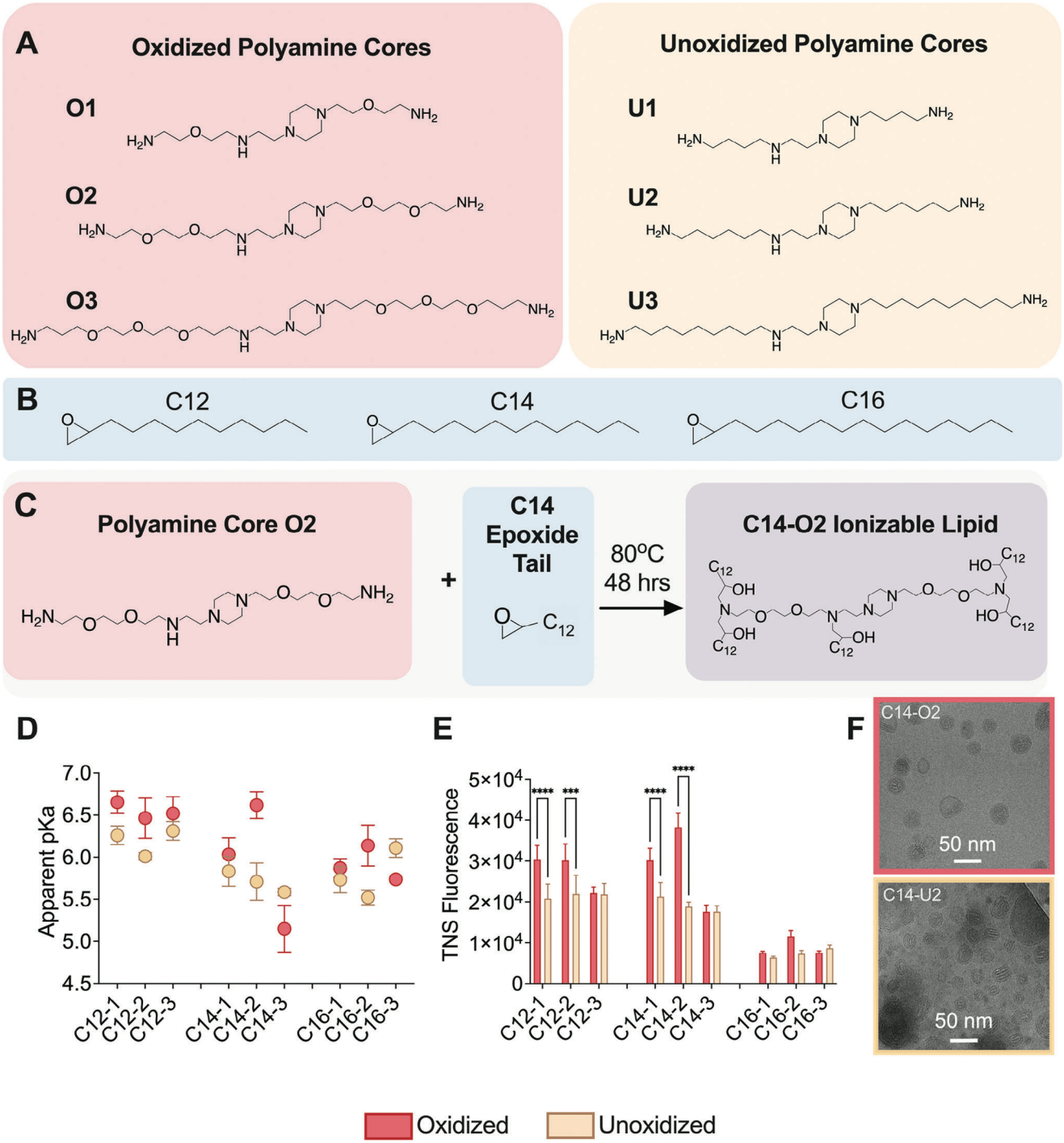


**Figure 2.** Oxidized and unoxidized ionizable lipids formulate into LNPs with different ionization and morphological properties. A) Oxidized or unoxidized polyamine cores were designed to test the role of ether spacers for mRNA delivery. B) Epoxide-terminated alkyl tails had a 12, 14, or 16-carbon alkyl chain. C) Epoxide tails from (B) and polyamine cores from (A) were combined in a 7:1 molar ratio via $S_N2$ reaction to synthesize a library of 18 ionizable lipids. D) p$K_a$ characterization and E) ionization energy for the 18 ionizable lipid library were measured by a 2-(p-toluidine)−6-naphthalenesulfonic acid (TNS) fluorescence assay. F) Representative cryo-TEM images of LNPs formulated with a C14-O2 ionizable lipid and its equivalent unoxidized ionizable lipid, C14-U2. TNS fluorescence intensities were compared using a two-way ANOVA with post hoc *t* tests using the Holm-Sidak correction. * $p < .05$, ** $p < .01$, *** $p < .001$, and **** $p < .0001$.

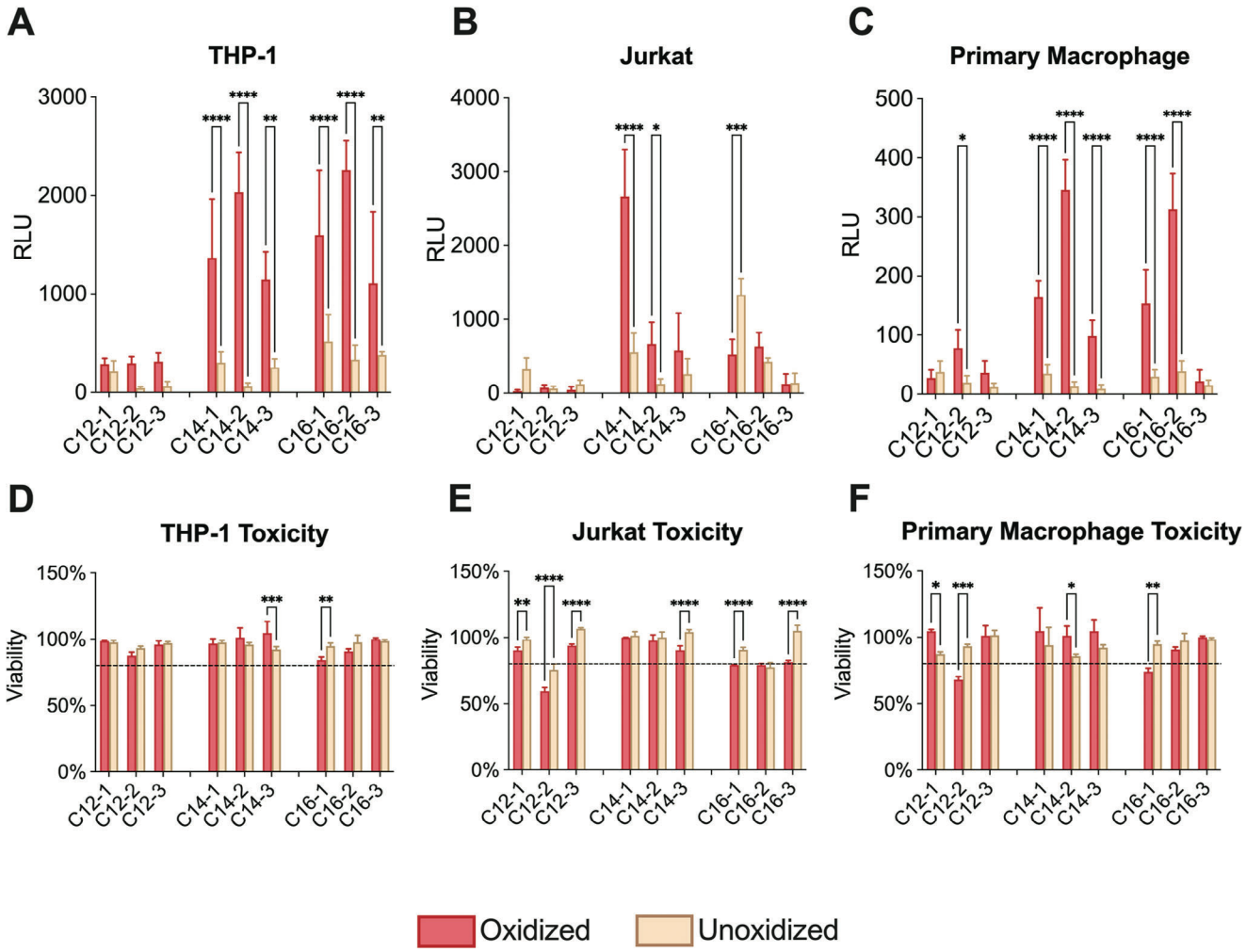


**Figure 3.** oLNPs deliver luciferase mRNA to phagocytes with higher potency than uLNP counterparts. A) THP-1 human macrophages were treated with luciferase mRNA LNPs at a dose of 200 ng per 60 000 cells. Luminescence was measured 24 h later. $n = 5$ biological replicates. B) Jurkat human T cells were treated with luciferase mRNA LNPs at a dose of 50 ng per 60 000 cells. Luminescence was measured 24 h later. $n = 5$ biological replicates. C) Donor-derived $CD14^+$ primary human monocytes were differentiated into macrophages after 7 d of culture in granulocyte-macrophage colony-stimulating factor(GMCSF)-supplemented medium. Macrophages were treated with luciferase mRNA LNPs at a dose of 200 ng per 60 000 cells. Luminescence was measured 24 h later. $n = 3$ independent donors. D) THP-1 human macrophages were treated with luciferase mRNA LNPs at a dose of 200 ng per 60 000 cells; cell viability was evaluated with a CellTiterGlo assay at 24 h. The luminescence signal was normalized to untreated cells. E) Jurkat human T cells were treated with luciferase mRNA LNPs at a dose of 50 ng per 60 000 cells; cell viability was evaluated with a CellTiterGlo assay at 24 h. F) Primary human macrophages were generated as in (B) and treated with luciferase mRNA LNPs at a dose of 200 ng per 60k cells; cell viability was evaluated with a CellTiterGlo assay at 24 h. $n = 3$ independent donors. The luminescence signal was normalized to untreated cells. All data are presented as the mean ± standard deviation and were analyzed using a two-way ANOVA with post hoc *t* tests using the Holm–Sidak correction. * $p < .05$, ** $p < .01$, *** $p < .001$, and **** $p < .0001$.

below the threshold for toxicity (Figure 3D–F). Notably, all LNPs utilizing C12- polyamines had significantly reduced mRNA delivery in comparison to C14- and C16- counterparts, regardless of physicochemical properties, indicating that shorter alkyl tail lengths may be detrimental to mRNA delivery to macrophages (Figure S4, Supporting Information).

Second, the ether groups can serve as additional sites for hydrogen bonding to occur with the mRNA cargo. Although the exact nature of the hydrogen bonding between the ionizable lipid and mRNA has not been elucidated, it is hypothesized that improvements in delivery between oLNPs and uLNPs can be partially explained by previous observation of the role of hydrogen bonding between ionizable lipid ether groups and the mRNA nucleobase, sugar, or backbone.[72] The differences in delivery seen between the O1, O2, and O3 LNPs suggest that the extent of hydrogen bonding possesses a degree of tunability, which potentially offers a route to optimize lipid-mRNA packing in terms of both organization and number of mRNAs per LNP within the LNP subcompartments and influence subsequent mRNA delivery.[72] This recently proposed structural hypothesis is relevant to this work; however, there are likely other contributing factors, and changes to hydrogen bonding potential are only one proposed explanation for the differences between these lipids. Future work employing advanced characterization techniques that

provide greater quantitative insight into LNP internal structure such as small angle X-ray scattering (SAXS) could be used to elucidate these mechanisms further.[72,73]

### 2.3. High Throughput In Vivo Screening of DNA-Barcoded oLNPs and uLNPs for Tropism to Immune Cells

To investigate how oLNPs performed in vivo compared to the uLNP library, we utilized a high throughput in vivo screening approach based on DNA barcoding to identify LNPs with tropism to immune cells after systemic administration. Here, we used the LNP library to encapsulate 61 nucleotide single-stranded DNA (ssDNA) barcodes, with each LNP formulation encapsulating a unique DNA barcode, thus aliasing the identity of the LNP with the sequence of the barcode. Since the chemical identity of an LNP is partially influenced by its cargo, the barcoded LNP library was formulated to co-encapsulate mCherry mRNA with the ssDNA barcode (10:1 by weight), to give the LNP "mRNA-like" characteristics and formulated with lipids at ratio of 35:16:46.5:2.5 ionizable lipid:DOPE:Chol:PEG-Lipid (mol%).[74,75] The final barcoded LNP library contained a total of 20 LNPs: 18 from the oLNP/uLNP library and additional gold standard C12-200 and MC3 control LNPs. All LNPs were characterized prior to injection and LNPs with a hydrodynamic radius > 200 nm or mRNA/barcode encapsulation < 30% were to be excluded from the injected pool to remove LNPs that could occlude fine vasculature and low-quality LNPs, respectively. None of the samples fell outside of the inclusion range, but all formulations had lower than expected encapsulation properties compared to LNPs encapsulating mRNA alone, likely due to the mixed nucleic acid cargo (Figure S4, Supporting Information). All 20 LNPs were pooled and delivered as a single 200 µL intravenous injection, a ten-fold dilution for each LNP. After 6 h, blood, spleen, and inguinal lymph nodes were harvested, processed into single-cell suspensions, and sorted using FACS by organ and cell type: monocytes/macrophages ($CD11b^+$), T cells ($CD3^+$), B cells ($CD19^+$), and dendritic cells ($CD83^+$). Barcodes were extracted from the isolated cell populations, amplified using PCR, and prepared for downstream barcode analysis via next-generation sequencing (NGS).

Barcode accumulation was measured in each of the organ and cell types, and enhanced tropism was assessed by quantifying the relative accumulation of each barcode in the injected pool within each sample. We identified LNPs that demonstrated significant enrichment within immune populations compared to the uninjected pooled LNP sample (**Figure 4B**); for each sample, the LNPs were scored from 1 to 20 based on their enrichment, and the scores across all samples were aggregated to assess overall enrichment (Figure 4C). In contrast to in vitro screens, the top performing LNPs included both oLNPs and uLNPs, suggesting the role of complex biotransformations in vivo, such as the binding of serum proteins and the formation of a protein corona and biotransformation by the liver, as partial determinants of particle tropism and stability.[76,77] Thus, tissue and cell specificities are not predictable from in vitro data alone, and inconsistencies between in vitro and in vivo screens are a long-standing challenge to the development of new nanoparticle therapies. The 3 top performing LNPs, LNP 14 (C16-O1), LNP 7 (C14-O2), and LNP 4 (C12-U2), primarily accumulated in spleen and blood tissues and C16-O1 were significantly enriched in nearly all samples, confirming the trends seen in the heat map (**Figure 5B,C**). For blood monocytes ($CD11b^{hi}$, $FSC^{low}$, $SSC^{low}$), only LNP 14 and LNP 4 were significantly enriched ($p = 0.0002$ and $p = 0.033$, respectively), with LNP 7 enriched, but not significantly ($p = 0.07$). Further, LNP 7 (C14-O2) was significantly enriched in splenic macrophages ($CD11b^+$) and dendritic cells ($CD83^+$), further highlighting the affinity for phagocytic myeloid cells previously demonstrated through in vitro screens. The control MC3 and C12-200 LNPs were found to be depleted across all organs and cell types investigated, coinciding with their well-established liver tropism upon systemic i.v. administration (Figure 5C).

### 2.4. Confirmation of Top Performing LNPs from Barcoded Screen for mRNA Delivery to Immune Cells

Once top-performing LNPs were identified from the barcoding screen, functional mRNA delivery was confirmed to validate LNPs that can both accumulate in the target tissues and deliver mRNA cargo to the cytosol. LNPs 14 (C16-O1), 7 (C14-O2), and 12 (C14-U3) were selected based on their enrichment profiles and rank order elucidated through the barcoded screen (Figure 4C). For each LNP, the oxidized or unoxidized counterpart was also selected for validation screening (i.e., C16-U1, C14-U2, and C14-O3) to assess any differences in mRNA delivery to immune cells related to oxidation state as observed during in vitro screening.

To assess mRNA delivery, each LNP was formulated to encapsulate mCherry mRNA and administered intravenously at a dose of 1 mg $kg^{-1}$; blood, spleen, and inguinal lymph nodes were harvested after 12 h. The LNPs mainly transfected cells in the blood and spleen, with undetectable delivery to immune cells residing in the inguinal lymph nodes (Figure 5). C14-O2 LNP (LNP 7) had the highest mRNA delivery to blood CD11b+ monocytes, with an average mCherry positivity rate of 4–5% and minimal delivery to other blood-resident immune cells (Figure 5C,F,I). LNP C16-O1 (LNP 14), which had the highest aggregated enrichment score in the barcoding screen, had minimal delivery to the investigated immune cell types within the blood (Figure 5B). C16-O1 LNP was outperformed by its uLNP counterpart C16-U1 across all organ and cell types but neither displayed a cell and tissue specificity similar to C14-O2 LNP.

Although the results of the mCherry validation screen seemingly contradict the results of the barcoding screen, it is important to note that a key limitation of DNA barcoding is that it measures tropism via the accumulation of barcodes in specific cells and tissues but does not measure or predict the degree to which cargo will be translated. Further, since the character of an LNP is strongly determined by its cargo, there are likely to be differences in bioactivity between LNP encapsulating barcoded ssDNA and mRNA as opposed to mRNA alone. Thus, utilizing barcoded screens to pare down the overall pool of LNPs to a small group of lead candidates for mRNA-based screening can be used to successfully identify LNPs with the desired tropism and delivery, as was accomplished here. Interestingly, when comparing the same set of LNPs for organ-level systemic delivery using luciferase-encoding mRNA instead of mCherry

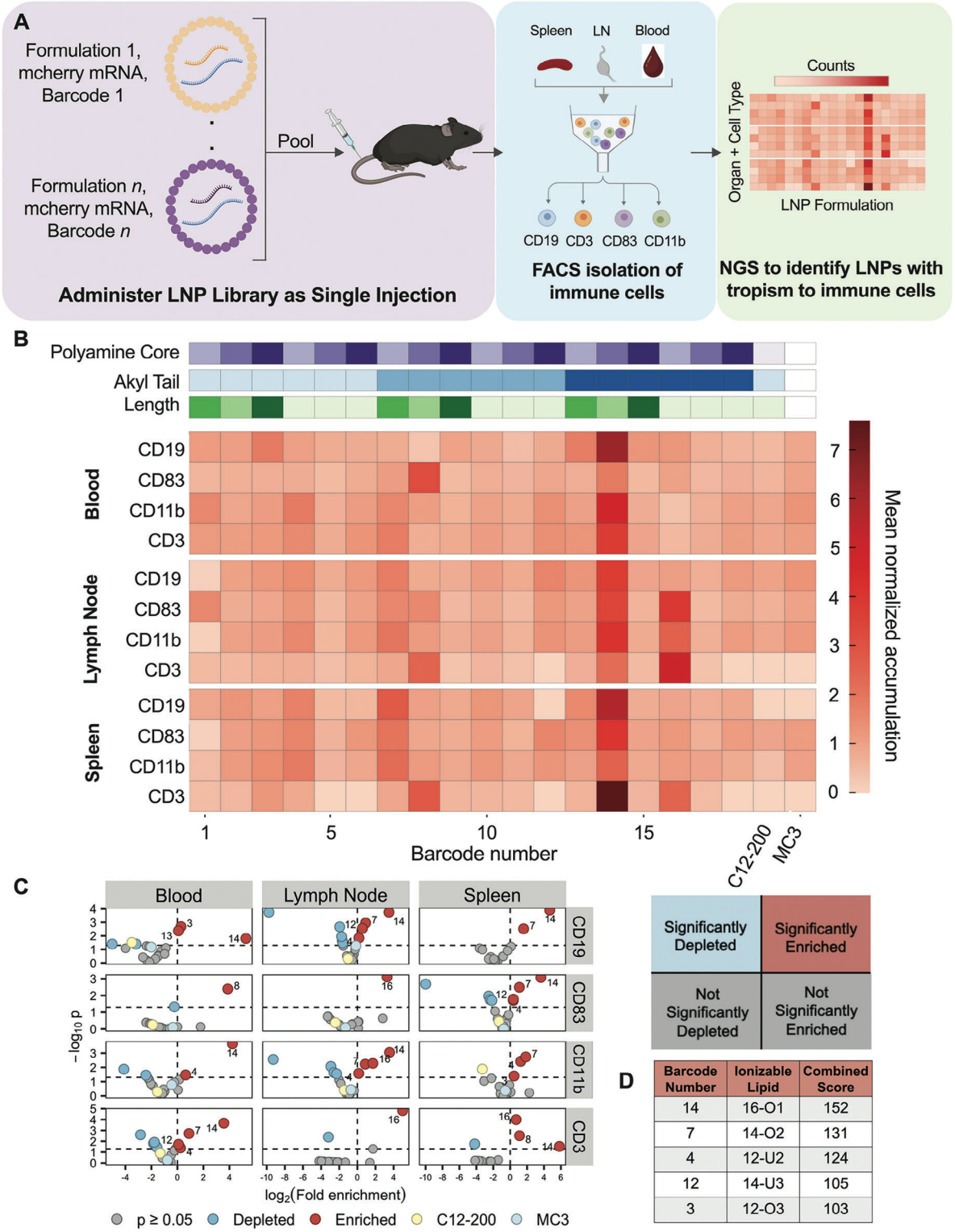


| Barcode Number | Ionizable Lipid | Combined Score |
|---|---|---|
| 14 | 16-O1 | 152 |
| 7 | 14-O2 | 131 |
| 4 | 12-U2 | 124 |
| 12 | 14-U3 | 105 |
| 3 | 12-O3 | 103 |

**Figure 4.** High throughput screening via DNA barcoding identifies oxidized LNPs with tropism to immune cells (B cells, T cells, dendritic cells, macrophages). A) Overview of barcoding experiment. Each LNP formulation encapsulated mCherry mRNA and a unique 61 nt DNA barcode. LNPs were pooled and injected into C57BL/6 mice via the tail vein and FACS was used to isolate immune cell populations. NGS identified LNPs with tropism to immune cell types. B) B cells ($CD19^+$), dendritic cells ($CD83^+$), macrophages ($CD11b^+$), and T cells ($CD3^+$) were isolated from the blood, lymph nodes, and spleen; barcode accumulation in cells was normalized to an uninjected pool of the barcoded LNP library. Each LNP formulation is represented as a column. $n = 5$ mice. C) Volcano plot enrichment diagrams comparing the statistical significance of enrichment or depletion of individual barcodes relative to the rest of the pool. D) Scoring of the barcoded library used to identify lead candidate LNPs for functional mRNA validation.

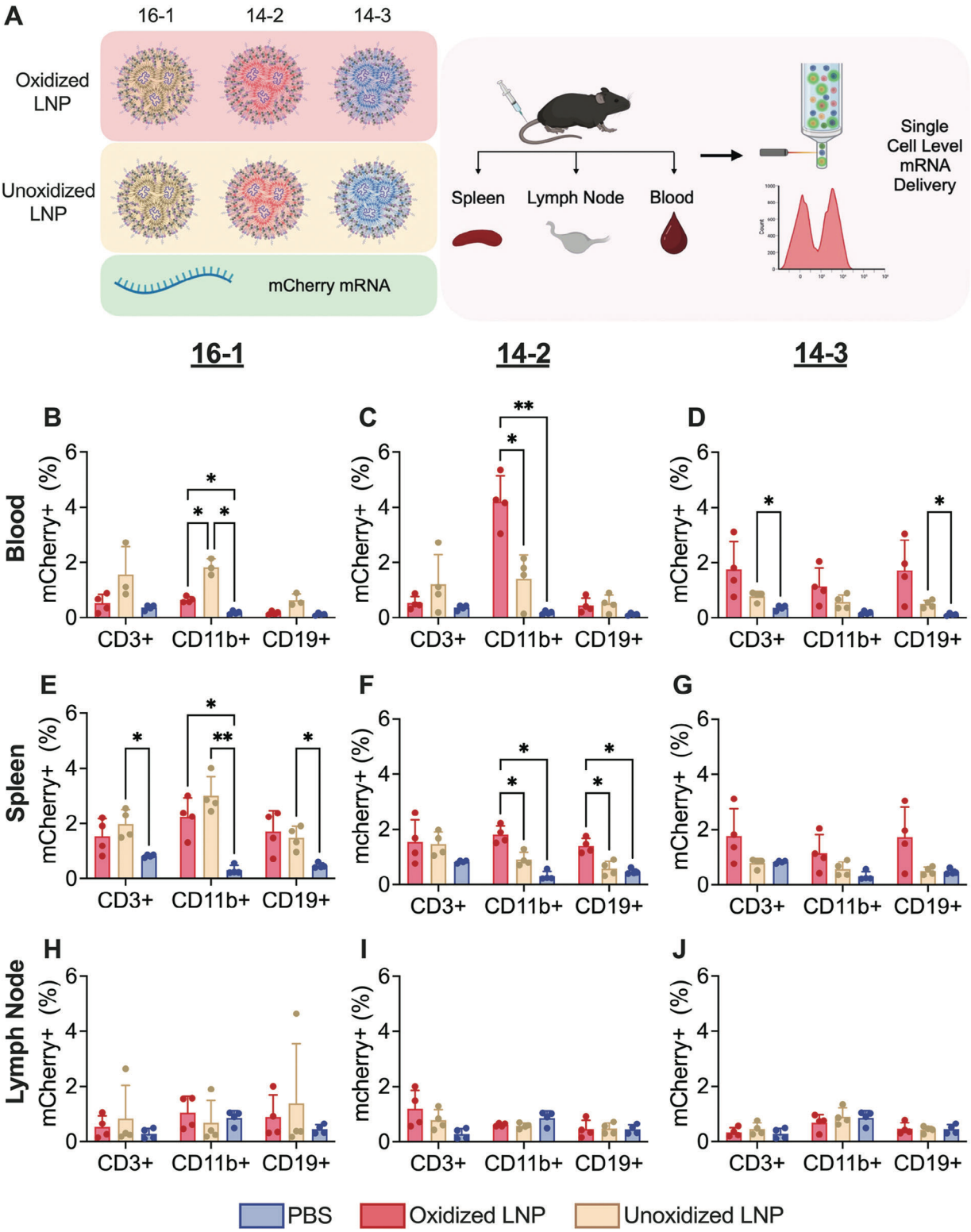


**Figure 5.** In vivo evaluation of mCherry mRNA LNPs identifies oxidized C14-O2 LNP with potent and selective delivery to monocytes. After DNA barcoding, 6 LNPs were evaluated for their ability to deliver mCherry mRNA in vivo. A) Overview of in vivo validation screen with mCherry mRNA. C57BL/6 mice were injected via the tail vein at a dose of 1 mg $kg^{-1}$ and organs were dissected 12 h post-injection. Immune cells were isolated from the spleen, lymph node, and blood, and mCherry expression was evaluated on a single cell level using flow cytometry. B–J) Transfection rates for each oLNP and uLNP pair in immune cells isolated from the blood (B–D), spleen (E–G), and inguinal lymph nodes (H–J). $n = 4$ mice. All data are presented as the mean ± standard deviation and were analyzed using a two-way ANOVA with post hoc $t$ tests using the Holm–Sidak correction. $^{*}$ $p < .05$ and $^{**}$ $p < .01$.

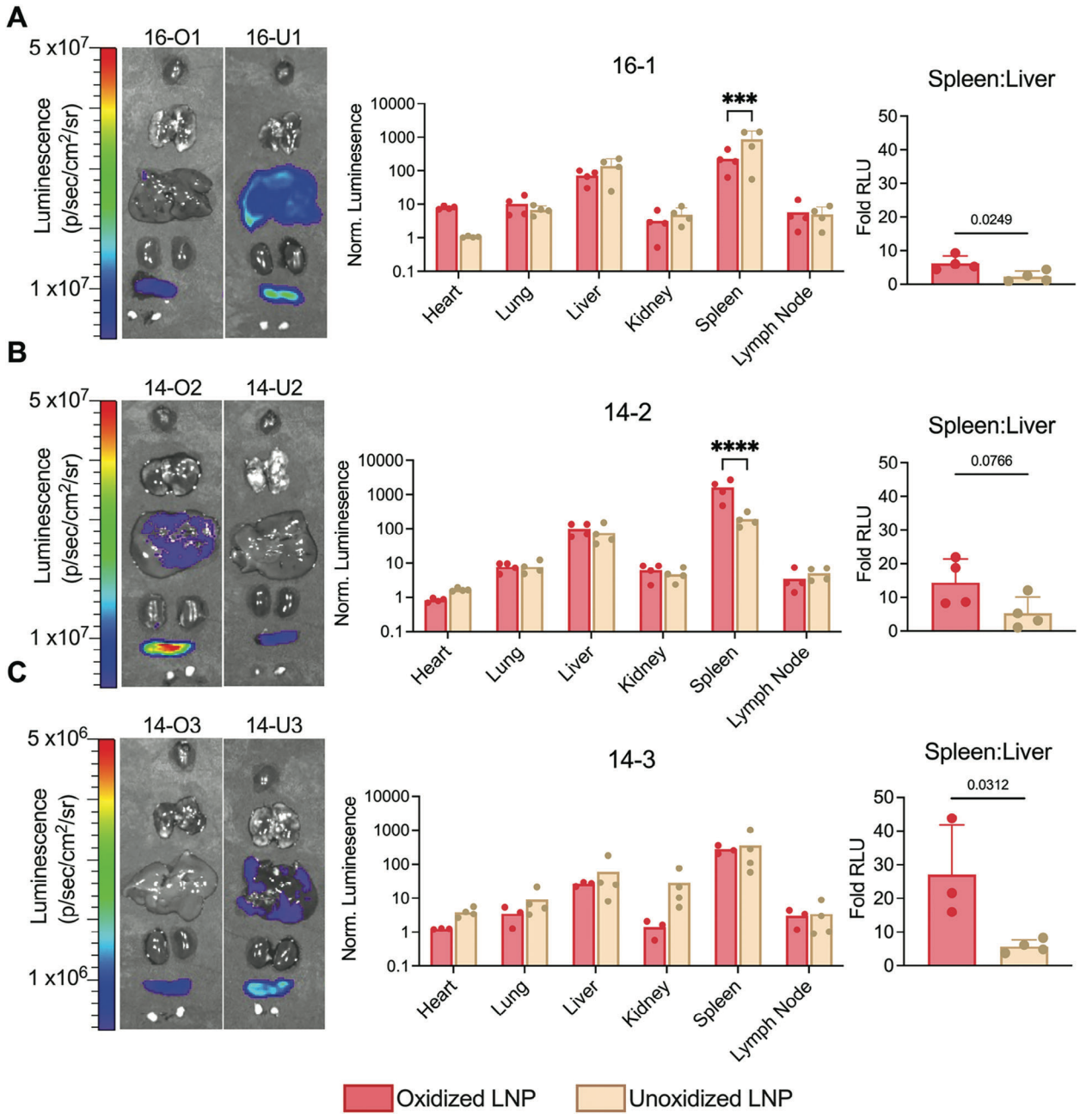


**Figure 6.** Whole body biodistribution of top LNPs indicates oxidized LNPs preferentially deliver luciferase mRNA to the spleen. A–C) Representative images (left), organ luminescence quantification (middle), and quantified ratio of spleen to liver luminescence (right) for the C16-1 LNPs (A), C14-2 LNPs (B), and C14-3 LNPs (C). C57BL/6 mice were injected via the tail vein at a dose of 5 μg mRNA per mouse. After 6 h, mice were sacrificed and major organs were harvested and analyzed for luciferase expression using IVIS imaging. $n = 3$–4 mice per group. Organs in IVIS images from top to bottom: heart, lungs, liver, kidneys, spleen, inguinal lymph nodes. The luminescence signal is normalized to phosphate buffer saline (PBS)-treated mice. All data are presented as the mean ± standard deviation. Organ luminescence was compared between oLNPs and uLNPs using a two-way ANOVA with post hoc *t* tests using the Holm–Sidak correction. $^{*}$ $p < .05$, $^{**}$ $p < .01$, $^{***}$ $p < .001$, and $^{****}$ $p < .0001$. Spleen:liver ratios were compared between oLNPs and uLNPs using an unpaired *t* test.

mRNA, there was minimal delivery to the liver and an observable shift in mRNA delivery toward the spleen when utilizing an oLNP compared to its equivalent uLNP, suggesting an ability for these LNPs to also reach non-immune cells within the spleen (**Figure** 6A–C). Previous works have demonstrated that changes in $pK_A$ as a result of additional charged lipid components can aid in preferential liver delivery; here, $pK_A$ was altered by the structure of the ionizable lipid component, resulting in preferential splenic delivery.[76] This further highlights trends not entirely captured through barcoded screens alone. However, through our validation screens, we identified C14-O2 LNP, which transfected monocytes with a high level of specificity relative to

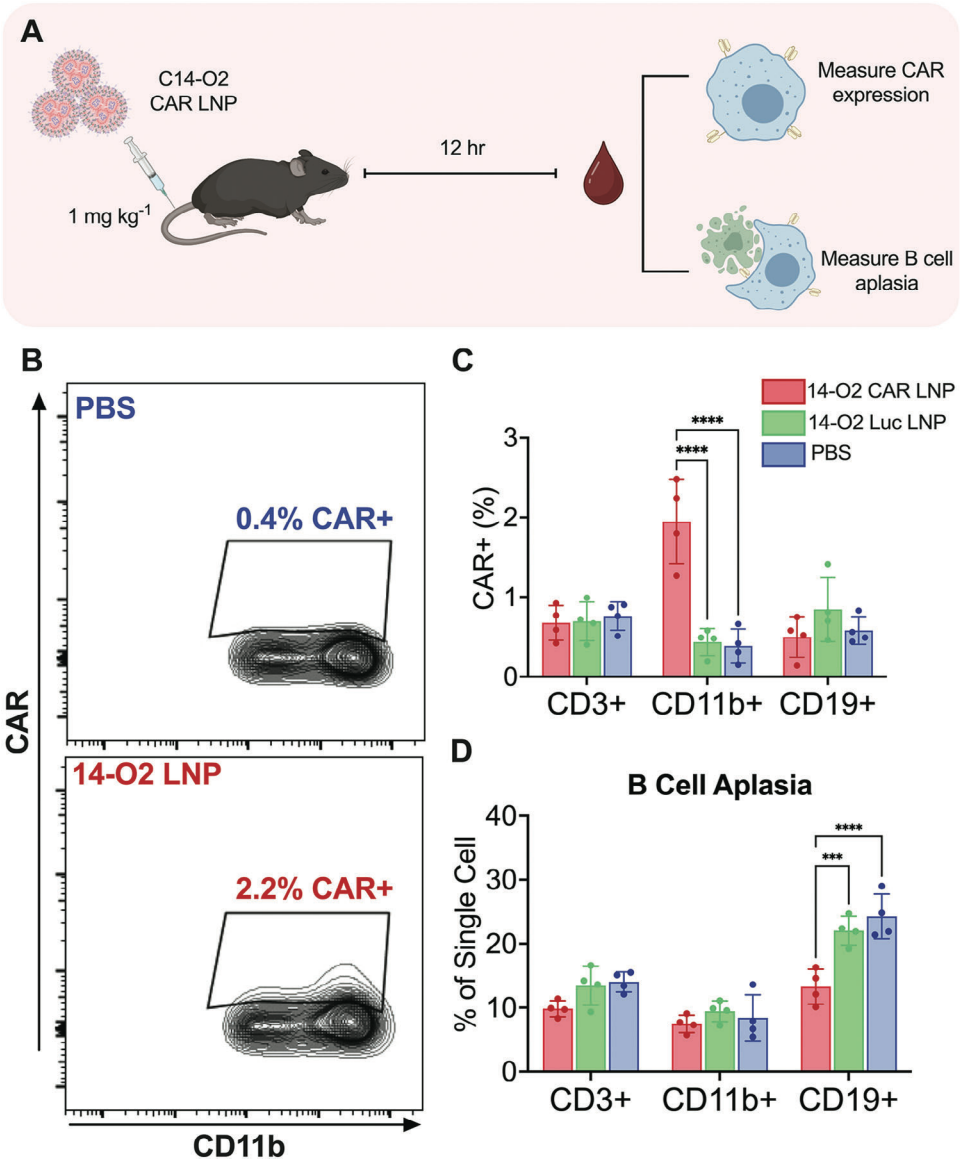


**Figure 7.** Oxidized C14-O2 LNP engineers functional CD19-CAR monocytes directly in situ and induces B cell aplasia. A) Experimental outline B) Representative flow cytometry plots and quantification (C) of CD19-CAR expression in blood monocytes isolated from mice treated with PBS or C14-O2 LNP encapsulating CD19-CAR mRNA. D) Healthy mice receiving CAR LNPs have significantly reduced $CD19^+$ blood B cells compared to mice receiving luciferase LNPs or PBS. C57BL/6 mice were injected via the tail vein at a dose of 1 mg $kg^{-1}$ and blood was collected 12 h post-injection. $n = 4$ mice per group. All data are presented as the mean ± standard deviation and were analyzed using a two-way ANOVA with Holm–Sidak correction. $^{*}$ $p < .05$, $^{**}$ $p < .01$, $^{***}$ $p < .001$, and $^{****}$ $p < .0001$.

other blood resident immune cells following systemic LNP administration.

### 2.5. In Situ Engineering of CAR Monocytes with C14-O2 LNP

Encouraged by the potency of the C14-O2 LNP to deliver mRNA to monocytes in vivo, we examined its ability to deliver an mRNA encoding a CD19-CAR to determine whether this LNP could be used to engineer CAR monocytes directly in situ. Here, CD19-targeted CAR was used as proof of concept for this engineering approach, as CAR function can be confirmed in healthy mice by measuring the elimination of blood $CD19^+$ B cells, referred to clinically as B cell aplasia. Mice were given a single injection of LNPs at a dose of 1 mg $kg^{-1}$ and sacrificed after 12 h. In mice receiving CAR mRNA LNPs, the specificity of the C14-O2 LNP was recapitulated, as CD19 CAR was detected in roughly 2% of circulating monocytes, with no detectable expression in $CD3^+$ T cells or $CD19^+$ B cells (**Figure** 7A,B). Further, circulating B cell counts were reduced by 45% compared to control mice injected with PBS, confirming the functionality of the encoded CAR (Figure 7C). Importantly, there was no significant difference in blood B cell counts between mice administered with a control luciferase mRNA C14-O2 LNP and mice administered with PBS, indicating that the LNP itself did not induce B cell aplasia or alter immune cell distributions. Thus, we confirmed the generation of

functional CD19-CAR monocytes using a single injection of our C14-O2 LNP.

The relatively low rate of CAR expression (2%) compared to mCherry (4%) from validation studies is likely due to two factors. First, CARs are complex macromolecules that have additional steps for expression and subsequent detection: namely, they must be transported from the cytosol and incorporated into the cell membrane.[78] This is compared to a mCherry protein that folds within the cytosol itself without any additional transport. Second, CARs are not recycled back to the cell surface after binding, meaning that the expression of the CAR via translation of the mRNA is in direct competition with the depletion of the CAR that occurs through binding events with CD19+ B cells.[79,80] Together, these phenomena can obfuscate the detection of the CAR, which informed the 12 h time point chosen for the in vivo CAR monocyte studies, as it enabled simultaneous detection of CAR functionality (B cell aplasia) and CAR expression. Due to the persistence of CAR expression at 12 h, it is expected that B cell aplasia would continue to increase over time. However, the measured B cell aplasia combined with the direct detection of the CAR confirms the presence and functionality of the CAR monocytes.

## 3. Conclusion

These studies explored the role of oxidation on the physicochemical properties and bioactivity of ionizable lipid nanoparticles, oLNPs. In vitro characterization of each class of LNPs revealed salient differences in ionization and morphological properties, which translated to differences in mRNA delivery to macrophages in vitro and ex vivo, a cell type that is particularly sensitive to these LNP characteristics. To assess differences upon systemic administration, DNA barcoding was used to identify LNPs with tropism to immune cells residing in major immune organs. Although there were no clear relationships between immune cell tropism and lipid oxidation state, follow-up studies of the top hits encapsulating luciferase and mCherry reporter mRNAs yielded interesting results. When using luciferase mRNA to measure whole organ biodistribution, oLNPs preferred extrahepatic delivery, specifically to the spleen, compared to uLNP counterparts, possibly indicating a role of differential binding of serum proteins such as ApoE and increased selectivity for immune cells such as macrophages. Second, mCherry-based validation studies identified an ionizable lipid, C14-O2, capable of potent and selective delivery of mRNA to blood monocytes. In a proof-of-concept study, a C14-O2 LNP was used to deliver a functional CD19-CAR mRNA and was shown to engineer functional CAR monocytes directly in situ, confirmed by the depletion of circulating $CD19^+$ B cells in healthy mice. In sum, these studies identify the role of oLNPs for mRNA delivery to phagocytes and extrahepatic organs and identify a platform LNP, C14-O2, which can be used for the therapeutic engineering of monocytes in situ.

## 4. Experimental Section

*Ionizable Lipid Synthesis*: Epoxide-terminated alkyl chains were mixed with polyamine cores at a 7:1 molar ratio and allowed to react for 48 h at 80 °C in an excess of ethanol. The product was dried using a Rotavapor R-300 (Buchi) to remove excess solvent, before being resuspended to a concentration of 40 mg $mL^{-1}$ in ethanol.

*Lipid Nanoparticle Formulation (LNP) and Characterization—Microfluidic Formulation of LNPs*: LNPs were formulated using microfluidic mixing of a lipid-containing ethanol phase and a mRNA-containing aqueous phase via a microfluidic device containing staggered herringbone micromixers. For in vitro screening of ionizable lipid libraries, the ethanol phase was prepared by combining ionizable lipid, 1,2-distearoyl-*sn*-glycero-3-phosphoethanolamine (DOPE, Avanti Polar Lipids), cholesterol (Sigma), or a lipid anchored polyethylene glycol (C14-PEG 2000, Avanti Polar Lipids) at a mol% of 35:16:46.5:2.5, respectively. The aqueous phase was prepared by diluting the appropriate mRNA to a concentration of .075 mg $mL^{-1}$ in 10 mM citrate buffer (pH 3). Ethanol and aqueous phases were mixed at 1:3 ratio using a single-channel staggered herringbone microfluidic mixing device. LNPs were subsequently collected in a 20 kDa MWCO dialysis cassette, dialyzed against 1x PBS for 2 h, and sterile filtered using a .22 µm syringe filter (Thermo).

*Lipid Nanoparticle Formulation (LNP) and Characterization—Physicochemical Characterization of LNPs*: Dynamic light scattering and zeta potential were measured in triplicate using a Zetasizer Nano (Malvern). mRNA content in LNP dispersions was measured using NanoDrop absorbance readings at 260 nm and 280 nm. mRNA encapsulation efficiency was measured using a RiboGreen assay (ThermoFisher) according to manufacturer protocols. LNP $pK_a$ was determined using a TNS-based fluorescence assay, as previously described.[47,62] Briefly, LNPs were diluted to a concentration of 20 ng mRNA $uL^{-1}$ in PBS, and 2.5 µL of this stock was diluted into a well containing 100 µL of buffer (150 mM sodium chloride, 20 mM sodium phosphate, 25 mM ammonium citrate, and 20 mM ammonium acetate) at pH ranging from 3.0 to 12.0. TNS reagent was added to each well to reach a final TNS concentration of 6 µM, incubated for 10 min, and the fluorescence signal of each well was measured at an excitation and emission wavelength of 322 nm and 431 nm respectively. Fluorescence values were fitted to a sigmoidal function and $pK_a$ was determined to be pH at which the inflection point occurred. Ionization energy was calculated to be the magnitude of the fluorescence signal at each pH.

*Cell Culture and In Vitro Biological Assays—THP-1 Monocyte Cell Culture and Luciferase Assays*: THP-1 monocytes were cultured in suspension at $2.5 \times 10^5$–$2 \times 10^6$ cells $mL^{-1}$ in Roswell Park Memorial Institute 1640 medium (RPMI) supplemented with 10% heat inactivated fetal bovine serum (FBS) and 1% penicillin/streptomycin. For luciferase assays, cells were pelleted and resuspended to a concentration of $5.0 \times 10^5$ cells $mL^{-1}$ in culture medium further supplemented with 10 ng $mL^{-1}$ of phorbol 12-myristate 13-acetate (PMA) and 100 µL of the suspension was added to each well of a 96-well plate ($5 \times 10^4$ cells per well). Cells were allowed to adhere for 48 h after plating before cells were refreshed with PMA-free medium and LNPs encapsulating luciferase-encoding mRNA were added at a dose of 200 ng mRNA per well (200 ng mRNA per 50k cells). After 24 h, luciferase (Luciferase Assay, Promega) or toxicity (CellTiter-Glo, Promega) assays were performed according to the manufacturer's protocol.

*Cell Culture and In Vitro Biological Assays—Jurkat T Cell Culture and Luciferase Assays*: Jurkat cells were cultured in suspension at $2.5 \times 10^5$–$2 \times 10^6$ cells $mL^{-1}$ in RPMI supplemented with 10% FBS and 1% penicillin-streptomycin. For luciferase assays, cells were pelleted and resuspended to a concentration of $6 \times 10^5$ cells $mL^{-1}$ in culture medium, and 100 µL of the suspension was added to each well of a 96-well plate ($6 \times 10^4$ cells per well). Cells were then immediately treated with LNPs encapsulating luciferase-encoding mRNA at a dose of 50 ng per well (50 ng per 60k cells). After 24 h, luciferase (Luciferase Assay, Promega) or toxicity (CellTiter-Glo, Promega) assays were performed according to the manufacturer's protocol.

*Cell Culture and In Vitro Biological Assays—Primary Human Macrophage Cell Culture and Luciferase Assays*: Primary human monocytes ($CD14^+$) were collected from healthy donor patients through the University of Pennsylvania Human Immunology Core. For luciferase and toxicity assays, cells were diluted to $5 \times 10^5$ cells $mL^{-1}$ in RPMI supplemented 10% FBS, 1% penicillin/streptomycin and 10 ng $mL^{-1}$ GMCSF (Peprotech, Cat: 300–03) and 100 µL of the suspension was added to each well of a 96-well plate

on day 0. Cells were refreshed with GMCSF-supplemented growth media on day 3 and treated with LNPs encapsulating luciferase-encoding mRNA at a dose of 200 ng mRNA per well (200 ng mRNA per 50k cells) on day 6. After 24 h, luciferase (Luciferase Assay, Promega) or toxicity (CellTiter-Glo, Promega) assays were performed according to the manufacturer's protocol.

*Animal Protocols*: All animal protocols were approved by the Institutional Animal Care and Use Committee of the University of Pennsylvania (#806 540), and all performed procedures were in accordance with the Guidelines for Care and Use of Laboratory Animals at the University of Pennsylvania.

*Barcoded Library Formulation and Characterization—Barcoded LNP Library Formulation*: LNPs were formulated to keep ionizable lipid:nucleic acid weight ratio constant. The oxidized/unoxidized ionizable lipid, C12-200, or MC3 ionizable lipid was added to an ethanol solution containing DOPE, cholesterol, and C14-PEG2000 (35:16:46.5:2.5, ionizable lipid:DOPE:Chol:PEG-Lipid, mol%) and mixed with an aqueous phase of citrate buffer (pH 3.0) containing mCherry mRNA and a unique ssDNA barcode using a staggered herringbone microfluidic mixing device. LNPs were subsequently collected in a 20 kDa MWCO dialysis cassette (Thermo), dialyzed against 1x PBS for 2 h, and sterile filtered using a .22 µm syringe filter.

*Barcoded Library Formulation and Characterization—Barcoded LNP Library Sizing*: LNPs were diluted 100X in PBS at pH 7.4, transferred to a polystyrene cuvette, and analyzed using dynamic light scattering (Malvern Nano ZS Zetasizer). Measurements were made in triplicate with 15 s run duration.

*Barcoded Library Formulation and Characterization—Barcoded LNP library mRNA and ssDNA Barcode Encapsulation Quantification*: Quant-iT RiboGreen (ThermoFisher) and Quant-iT OliGreen assay (ThermoFisher) manufacturer protocols were modified to include DNAse I and RNAse A respectively to separately quantify mRNA and b-DNA and minimize signal cross-contamination during detection of encapsulated cargo.

*Barcoded Library Formulation and Characterization—Processing of Organs into Single Cell Suspensions for Fluorescence Activated Cell Sorting (FACS) and Flow Cytometry*: The pooled LNPs were administered as a single 200 µL tail vein injection. 6 h following injection, mice were sacrificed and blood (≈500 µL), spleen, and inguinal lymph nodes were harvested.

The spleen was processed into a single-cell suspension by mechanically disrupting the organ on a 70 µm cell strainer. The strainer was rinsed with 1 mL of PBS and the flow-through was collected, passed through the strainer 3 times, and diluted into 4 mL of Ammonium-chloride-potassium (ACK) Lysing Buffer (Thermo, Cat: U1049201). The solution was then centrifuged at 800*g* for 5 min and the cell pellet was resuspended in 3 mL of PBS + .1% BSA and stored on ice until sorting.

The entire blood sample was diluted into 1 mL of ACK Lysing Buffer to lyse red blood cells. After a 5 min incubation, the suspension was centrifuged at 800*g* for 5 min, the supernatant was aspirated, and the pellet was resuspended back into lysing buffer. This process was repeated 5–7 times until a white cell pellet in a clear supernatant was visible. Once clear, the supernatant was aspirated, and the pellet was resuspended in 1 mL of PBS + .1% BSA and stored on ice until sorting.

Lymph nodes were processed into a single-cell suspension using mechanical disruption in PBS + .1% BSA. The suspension was then passed through a 70 µm cell strainer 3x and the flowthrough was collected, pelleted at 800*g* for 5 min, and resuspended in 300 µL of PBS + .1% BSA and stored on ice until sorting.

*Sequencing Library Preparation for Barcoding Experiment—FACS of Immune Cells*: Single-cell suspensions of the blood, spleen, and lymph nodes were stained with Pacific Blue anti-CD3 (1:100, Biolegend, Cat: 100 214), Alexa Fluor 700 anti-CD11b (1:100, Biolegend, Cat: 101 222), FITC anti-CD19 (1:100, Biolegend, Cat: 101 506), and PE anti-CD83 (1:100, Biolegend, Cat: 121 508). Data for compensations were acquired using single stained spleen samples from mice injected with PBS and mCherry total compensation beads (Takara, Cat: 632 595). Samples were sorted using an AriaFusion ES (BD Biosciences). For each organ, the entire sample was sorted into CD3, CD19, CD11b, or CD83 populations.

*NGS Library Pool Preparation*: Cells were sorted into a DNA-stabilizing lysis buffer containing 100 mM tris-HCl, 4 mM EDTA, 0.2% sodium dodecyl sulfate (SDS), and 200 mM NaCl. To remove protein and RNA contaminants, 20 µg of RNase A (New England Biolabs) and 100 µg of proteinase K (New England Biolabs) were added to each sample. Barcoded DNA (b-DNA) was subsequently extracted using a Monarch PCR & DNA Cleanup Kit (New England Biolabs), following the provided protocol modification for ssDNA isolation. Extracted b-DNA was amplified by PCR using Q5 High-Fidelity DNA Polymerase (New England Biolabs) using overhanging primers to add adapter (P5/P7) and index (i7) sequences for Illumina sequencing. Resultant libraries were pooled by tissue source and fragments separated by agarose gel electrophoresis. The 144 bp product (library pool) was excised from the gel and purified using a Monarch DNA Gel Extraction Kit (New England Biolabs) following the manufacturer's instructions. The concentration of resultant pools was quantified using a Qubit 1X dsDNA High Sensitivity assay on a Qubit Flex fluorometer (Thermo Fisher Scientific). Pools were combined in equimolar amounts to produce a complete library pool for next-generation sequencing (NGS), which was stored at −20 °C until sequencing. NGS was performed using an Illumina MiSeq series sequencer (RRID:SCR_02 2382) with a 5% PhiX Sequencing Control (Illumina) spike-in.

*NGS Data Analysis*: Demultiplexed FASTQ files were processed using the UMI-tools Python package to extract unique molecular identifiers (UMI) and barcode sequences.[81] All analysis downstream of sequence extraction used a combination of shell (sh) scripting and R scripts, using the GNU Core Utilities and an assortment of packages available from the Comprehensive R Archive Network (CRAN).[82–95] The Nix package manager (with pinned nixpkgs revision 9cd622d) was used for dependency management to maximize reproducibility.[96]

*Delivery of mRNA to Monocytes In Vivo Following Intravenous Administration—mCherry Validation Study*: 16-O1, 16-U1, 14-O2, 14-U2, 14-O3, and 14-U3 LNPs were formulated at 10:1 ionizable lipid:mCherry mRNA weight ratio using the above microfluidic mixing technique. LNPs were administered via tail vein injection to 6–8 week old C57BL/6 mice at a dose of 1 mg mRNA $kg^{-1}$ body weight. After 12 h, mice were sacrificed and peripheral blood, spleens, and inguinal lymph nodes were collected. Organs were processed into single-cell suspensions in a similar manner to barcoding samples, and cells were stained with Alexa Fluor 700 anti-CD3 (1:100, Invitrogen, Cat: 5 016 842), Alexa Fluor 488 anti-CD11b (1:100, Invitrogen, Cat: 5 016 687), and eFluor 450 anti-CD19 (1:100, Invitrogen, Cat: 501 129 357). Compensation samples were acquired using single stained blood samples from mice injected with PBS and mCherry total compensation beads (Takara, Cat: 632 595).

*Delivery of mRNA to Monocytes In Vivo Following Intravenous Administration—Luciferase Validation Study*: 16-O1, 16-U1, 14-O2, 14-U2, 14-O3, and 14-U3 LNPs were formulated at 10:1 ionizable lipid:luciferase mRNA weight ratio using the above microfluidic mixing technique. LNPs were administered via tail vein injection to 6–8 week old C57BL/6 mice at a dose of 1 mg mRNA $kg^{-1}$ body weight. After 6 h, mice were injected with 200 µL of a luciferin salt solution (15 mg $mL^{-1}$) intraperitoneally. Mice were sacrificed after 10 min and the heart, lungs, spleen, liver, kidneys, and inguinal lymph nodes were harvested and imaged for bioluminescence using an IVIS Spectrum (Perkin Elmer).

*Delivery of mRNA to Monocytes In Vivo Following Intravenous Administration—In Situ Engineering of CAR Monocytes*: 14-O2 LNPs were formulated at a 10:1 ionizable lipid:CD19-CAR mRNA or luciferase mRNA weight ratio using the above microfluidic mixing technique. LNPs were administered via tail vein injection to 6–8 week old C57BL/6 mice at a dose of 1 mg mRNA $kg^{-1}$ body weight. After 10 h, peripheral blood was drawn using a retroorbital eye bleed and was processed into a single-cell suspension using the previously established protocol. For CAR staining, Fc receptors were blocked using murine TruStain FcX (Biolegend) according to manufacturer protocols. CD19-CAR was stained using a primary murine His-tagged CD19 protein (Sino Biological, Cat: 50510-M08H-B) followed by staining with secondary APC anti-His antibody (R&D Systems, Cat: MAB050). Cells were subsequently stained for immunophenotyping using the same panel and dilutions as the mCherry-based validation

study. Compensations were acquired using single stained blood samples from mice injected with PBS and AbC Compensation Beads reacted with the CAR secondary antibody (Molecular Probes, Cat: U10497).

*Statistical Analysis*: All statistical analyses were performed as specified in each figure caption using GraphPad Prism version 10.0.0 for Mac, GraphPad Software, Boston, Massachusetts USA, graphpad.com.

For in vitro luciferase and viability assays, data were normalized to untreated cells, and mean luminescence ± standard deviation was plotted. For TNS assays to quantify $pK_a$, fluorescence values were normalized to the highest TNS signal before being fit to a sigmoidal function. For TNS assays to quantify ionization energy, the gain was manually set, and raw fluorescence values were reported.

For in vivo luminescence imaging, the luminescence signal was normalized to PBS control mice, and the mean luminescence ± standard deviation was plotted. For in vivo flow cytometry studies, $mCherry^+$ or $CAR^+$ gates were set relative to mice receiving PBS. Gates for specific cell populations were set relative to unstained controls after compensation.

## Supporting Information

Supporting Information is available from the Wiley Online Library or from the author.

## Conflict of Interest

A.J.M. and M.J.M. have filed a patent application based on this work. The other authors declare no competing interests.

## Data Availability Statement

The data that support the findings of this study are available from the corresponding author upon reasonable request.

## Keywords

Immunotherapy, macrophage, mRNA, nanomedicine

Received: November 17, 2023
Revised: January 22, 2024
Published online:

[1] S. J. Schuster, J. Svoboda, E. A. Chong, S. D. Nasta, A. R. Mato, Ö. Anak, J. L. Brogdon, I. Pruteanu-Malinici, V. Bhoj, D. Landsburg, M. Wasik, B. L. Levine, S. F. Lacey, J. J. Melenhorst, D. L. Porter, C. H. June, *N. Engl. J. Med.* **2017**, *377*, 2545.
[2] J. H. Park, I. Rivière, M. Gonen, X. Wang, B. Sénéchal, K. J. Curran, C. Sauter, Y. Wang, B. Santomasso, E. Mead, M. Roshal, P. Maslak, M. Davila, R. J. Brentjens, M. Sadelain, *N. Engl. J. Med.* **2018**, *378*, 449.
[3] S. S. Neelapu, S. Tummala, P. Kebriaei, W. Wierda, C. Gutierrez, F. L. Locke, K. V. Komanduri, Y. Lin, N. Jain, N. Daver, J. Westin, A. M. Gulbis, M. E. Loghin, J. F. de Groot, S. Adkins, S. E. Davis, K. Rezvani, P. Hwu, E. J. Shpall, *Nat. Rev. Clin. Oncol.* **2018**, *15*, 47.
[4] S. L. Maude, T. W. Laetsch, J. Buechner, S. Rives, M. Boyer, H. Bittencourt, P. Bader, M. R. Verneris, H. E. Stefanski, G. D. Myers, M. Qayed, B. De Moerloose, H. Hiramatsu, K. Schlis, K. L. Davis, P. L. Martin, E. R. Nemecek, G. A. Yanik, C. Peters, A. Baruchel, N. Boissel, F. Mechinaud, A. Balduzzi, J. Krueger, C. H. June, B. L. Levine, P. Wood, T. Taran, M. Leung, K. T. Mueller, et al., *N. Engl. J. Med.* **2018**, *378*, 439.
[5] CAR T Cells: Engineering Immune Cells to Treat Cancer – NCI, https://www.cancer.gov/about-cancer/treatment/research/car-t-cells, (accessed: August 2023).
[6] K. Kirtane, H. Elmariah, C. H. Chung, D. Abate-Daga, *J Immunother Cancer* **2021**, *9*, e002723.
[7] N. Schaft, *Cancers* **2020**, *12*, 2567.
[8] A. Ukidve, K. Cu, N. Kumbhojkar, J. Lahann, S. Mitragotri, *Drug Deliv* **2021**, *11*, 2276.
[9] G. L. Beatty, M. O'Hara, *Pharmacol. Ther.* **2016**, *166*, 30.
[10] S. Rafiq, C. S. Hackett, R. J. Brentjens, *Nat. Rev. Clin. Oncol.* **2020**, *17*, 147.
[11] Global Manufacturing of CAR T Cell Therapy: Molecular Therapy – Methods & Clinical Development, https://www.cell.com/molecular-therapy-family/methods/fulltext/S2329-0501(16)30202-9?sf77801175=1, (accessed: August 2023).
[12] S. R. Bailey, T. R. Berger, C. Graham, R. C. Larson, M. V. Maus, *Eur. J. Immunol.* **2023**, *53*, 2250039.
[13] L. Cassetta, J. W. Pollard, *Nat. Rev. Drug Discov.* **2018**, *17*, 887.
[14] A. Canella, P. Rajappa, *Cancer Gene Ther.* **2023**, *30*, 964.
[15] S. Goswami, S. Anandhan, D. Raychaudhuri, P. Sharma, *Nat. Rev. Immunol.* **2023**, *23*, 106.
[16] L. Yang, Y. Zhang, *J. Hematol. Oncol.* **2017**, *10*, 58.
[17] Y. Wang, K. C. C. Johnson, M. E. Gatti-Mays, Z. Li, *J. Hematol. Oncol.* **2022**, *15*, 118.
[18] S. Wang, Y. Yang, P. Ma, H. Huang, Q. Tang, H. Miao, Y. Fang, N. Jiang, Y. Li, Q. Zhu, W. Tao, Y. Zha, N. Li, *Mol Ther Oncolytics* **2022**, *24*, 799.
[19] C. E. Olingy, H. Q. Dinh, C. C. Hedrick, *J. Leukoc. Biol.* **2019**, *106*, 309.
[20] T. Hourani, J. A. Holden, W. Li, J. C. Lenzo, S. Hadjigol, N. M. O'Brien-Simpson, *Front. Oncol.* **2021**, *11*, 788365.
[21] R. Noy, J. W. Pollard, *Immunity* **2014**, *41*, 49.
[22] G. Escobar, D. Moi, A. Ranghetti, P. Ozkal-Baydin, M. L. Squadrito, A. Kajaste-Rudnitski, A. Bondanza, B. Gentner, M. De Palma, R. Mazzieri, L. Naldini, *Sci. Transl. Med.* **2014**, *6*, 217ra3.
[23] H. Wu, S. Amirfakhri, H.-H. Lin, H. Hollandsworth, F. Filemoni, Y. Liu, Y. Wu, J. Y. S. Li, H. Xu, S. Chien, M. Bouvet, Y. Wang, *Bioeng. Transl. Med.* **2022**, *7*, e10285.
[24] A. Mucci, G. Antonarelli, C. Caserta, F. M. Vittoria, G. Desantis, R. Pagani, B. Greco, M. Casucci, G. Escobar, L. Passerini, N. Lachmann, F. Sanvito, M. Barcella, I. Merelli, L. Naldini, B. Gentner, *EMBO Mol. Med.* **2021**, *13*, 13598.
[25] F. Birocchi, M. Cusimano, F. Rossari, S. Beretta, P. M. V. Rancoita, A. Ranghetti, S. Colombo, B. Costa, P. Angel, F. Sanvito, M. Callea, R. Norata, L. Chaabane, T. Canu, A. Spinelli, M. Genua, R. Ostuni, I. Merelli, N. Coltella, L. Naldini, *Sci. Transl. Med.* **2022**, *14*, eabl4106.
[26] N. Anderson, M. Klichinsky, K. Ciccaglione, S. Pierini, B. Shah, A. Worth, R. Gabbasov, B. Menchel, D. Blumenthal, S. DeLong, S. Abramson, T. Condamine, *J. ImmunoTher. Cancer* **2022**, *10*, 0194.
[27] D. R. Deyle, D. W. Russell, *Curr. Opin. Mol. Ther.* **2009**, *11*, 442.
[28] D. M. McCarty, S. M. Young, R. J. Samulski, *Annu. Rev. Genet.* **2004**, *38*, 819.
[29] A. Ciuffi, *Curr. Gene Ther.* **2008**, *8*, 419.
[30] D. A. Kuzmin, M. V. Shutova, N. R. Johnston, O. P. Smith, V. V. Fedorin, Y. S. Kukushkin, J. C. M. van der Loo, E. C. Johnstone, *Nat. Rev. Drug Discov.* **2021**, *20*, 173.
[31] K. Bulaklak, C. A. Gersbach, *Nat. Commun.* **2020**, *11*, 5820.
[32] Z. Zhao, A. C. Anselmo, S. Mitragotri, *Bioeng. Transl. Med.* **2021**, *7*, e10258.
[33] S. A. Richman, S. Nunez-Cruz, B. Moghimi, L. Z. Li, Z. T. Gershenson, Z. Mourelatos, D. M. Barrett, S. A. Grupp, M. C. Milone, *Cancer Immunol. Res.* **2018**, *6*, 36.
[34] F. C. Thistlethwaite, D. E. Gilham, R. D. Guest, D. G. Rothwell, M. Pillai, D. J. Burt, A. J. Byatte, N. Kirillova, J. W. Valle, S. K. Sharma, K.

A. Chester, N. B. Westwood, S. E. R. Halford, S. Nabarro, S. Wan, E. Austin, R. E. Hawkins, *Cancer Immunol. Immunother.* **2017**, *66*, 1425.
[35] R. A. Morgan, J. C. Yang, M. Kitano, M. E. Dudley, C. M. Laurencot, S. A. Rosenberg, *Mol. Ther.* **2010**, *18*, 843.
[36] K. I. Berns, N. Muzyczka, *Hum. Gene Ther.* **2017**, *28*, 308.
[37] X. Xiao, J. Li, R. J. Samulski, *J. Virol.* **1996**, *70*, 8098.
[38] Y. Wang, C. Li, J. Xia, P. Li, J. Cao, B. Pan, X. Tan, H. Li, K. Qi, X. Wang, M. Shi, G. Jing, Z. Yan, H. Cheng, F. Zhu, H. Sun, W. Sang, D. Li, X. Zhang, Z. Li, J. Zheng, A. Liang, J. Zhou, K. Xu, *Blood Adv.* **2021**, *5*, 5290.
[39] L. R. Baden, H. M. El Sahly, B. Essink, K. Kotloff, S. Frey, R. Novak, D. Diemert, S. A. Spector, N. Rouphael, C. B. Creech, J. McGettigan, S. Khetan, N. Segall, J. Solis, A. Brosz, C. Fierro, H. Schwartz, K. Neuzil, L. Corey, P. Gilbert, H. Janes, D. Follmann, M. Marovich, J. Mascola, L. Polakowski, J. Ledgerwood, B. S. Graham, H. Bennett, R. Pajon, C. Knightly, et al., *N. Engl. J. Med.* **2021**, *384*, 403.
[40] E. E. Walsh, R. W. Frenck, A. R. Falsey, N. Kitchin, J. Absalon, A. Gurtman, S. Lockhart, K. Neuzil, M. J. Mulligan, R. Bailey, K. A. Swanson, P. Li, K. Koury, W. Kalina, D. Cooper, C. Fontes-Garfias, P.-Y. Shi, Ö. Türeci, K. R. Tompkins, K. E. Lyke, V. Raabe, P. R. Dormitzer, K. U. Jansen, U. Sahin, W. C. Gruber, *N. Engl. J. Med.* **2020**, *383*, 2439.
[41] N. Pardi, S. Tuyishime, H. Muramatsu, K. Kariko, B. L. Mui, Y. K. Tam, T. D. Madden, M. J. Hope, D. Weissman, *J. Control. Release* **2015**, *217*, 345.
[42] E. Kenjo, H. Hozumi, Y. Makita, K. A. Iwabuchi, N. Fujimoto, S. Matsumoto, M. Kimura, Y. Amano, M. Ifuku, Y. Naoe, N. Inukai, A. Hotta, *Nat. Commun.* **2021**, *12*, 7101.
[43] G. L. Beatty, A. R. Haas, M. V. Maus, D. A. Torigian, M. C. Soulen, G. Plesa, A. Chew, Y. Zhao, B. L. Levine, S. M. Albelda, M. Kalos, C. H. June, *Cancer Immunol. Res.* **2014**, *2*, 112.
[44] H. G. Caruso, H. Torikai, L. Zhang, S. Maiti, J. Dai, K.-A. Do, H. Singh, H. Huls, D. A. Lee, R. E. Champlin, A. B. Heimberger, L. J. N. Cooper, *J. Immunother.* **2016**, *39*, 205.
[45] Z. Ye, J. Chen, X. Zhao, Y. Li, J. Harmon, C. Huang, J. Chen, Q. Xu, *ACS Biomater. Sci. Eng.* **2022**, *8*, 722.
[46] J. G. Rurik, I. Tombácz, A. Yadegari, P. O. Méndez Fernández, S. V. Shewale, L. Li, T. Kimura, O. Y. Soliman, T. E. Papp, Y. K. Tam, B. L. Mui, S. M. Albelda, E. Puré, C. H. June, H. Aghajanian, D. Weissman, H. Parhiz, J. A. Epstein, *Science* **2022**, *375*, 91.
[47] M. M. Billingsley, N. Singh, P. Ravikumar, R. Zhang, C. H. June, M. J. Mitchell, *Nano Lett.* **2020**, *20*, 1578.
[48] M. Bernstein, *Clinical Pharmacology Considerations for Antibody-Drug Conjugates* **2022**.
[49] G. S. Naidu, S.-B. Yong, S. Ramishetti, R. Rampado, P. Sharma, A. Ezra, M. Goldsmith, I. Hazan-Halevy, S. Chatterjee, A. Aitha, D. Peer, *Adv. Sci.* **2023**, *10*, 2301929.
[50] D. Aldarondo, E. Wayne, *Adv. Drug Deliv. Rev.* **2022**, *182*, 114116.
[51] J. Zhang, S. Nie, Y. Zu, M. Abbasi, J. Cao, C. Li, D. Wu, S. Labib, G. Brackee, C.-L. Shen, S. Wang, *J. Control. Release* **2019**, *303*, 263.
[52] R. Duivenvoorden, J. Tang, D. P. Cormode, A. J. Mieszawska, D. Izquierdo-Garcia, C. Ozcan, M. J. Otten, N. Zaidi, M. E. Lobatto, S. M. van Rijs, B. Priem, E. L. Kuan, C. Martel, B. Hewing, H. Sager, M. Nahrendorf, G. J. Randolph, E. S. G. Stroes, V. Fuster, E. A. Fisher, Z. A. Fayad, W. J. M. Mulder, *Nat. Commun.* **2014**, *5*, 3065.
[53] C. Gao, Q. Huang, C. Liu, C. H. T. Kwong, L. Yue, J.-B. Wan, S. M. Y. Lee, R. Wang, *Nat. Commun.* **2020**, *11*, 2622.
[54] N. V. Mushenkova, E. E. Bezsonov, V. A. Orekhova, T. V. Popkova, A. V. Starodubova, A. N. Orekhov, *Biomedicines* **2021**, *9*, 915.
[55] C. Khatana, N. K. Saini, S. Chakrabarti, V. Saini, A. Sharma, R. V. Saini, A. K. Saini, *Oxid. Med. Cell Longev.* **2020**, *2020*, 1.
[56] S. Parthasarathy, A. Raghavamenon, M. O. Garelnabi, N. Santanam, *Methods Mol. Biol.* **2010**, *610*, 403.
[57] K. A. Whitehead, J. Matthews, P. H. Chang, F. Niroui, J. R. Dorkin, M. Severgnini, D. G. Anderson, *ACS Nano* **2012**, *6*, 6922.
[58] J. E. Dahlman, K. J. Kauffman, Y. Xing, T. E. Shaw, F. F. Mir, C. C. Dlott, R. Langer, D. G. Anderson, E. T. Wang, *Proc. Natl. Acad. Sci. U. S. A.* **2017**, *114*, 2060.
[59] M. P. Lokugamage, C. D. Sago, J. E. Dahlman, *Curr. Opin. Biomed. Eng.* **2018**, *7*, 1.
[60] A. J. Da Silva Sanchez, C. Dobrowolski, A. Cristian, E. S. Echeverri, K. Zhao, M. Z. C. Hatit, D. Loughrey, K. Paunovska, J. E. Dahlman, *Nano Lett.* **2022**, *22*, 4822.
[61] R. El-Mayta, R. Zhang, S. J. Shepherd, F. Wang, M. M. Billingsley, V. Dudkin, D. Klein, H. D. Lu, M. J. Mitchell, *Adv. Ther.* **2021**, *4*, 2000111.
[62] K. A. Hajj, R. L. Ball, S. B. Deluty, S. R. Singh, D. Strelkova, C. M. Knapp, K. A. Whitehead, *Small* **2019**, *15*, 1805097.
[63] S. Li, Y. Hu, A. Li, J. Lin, K. Hsieh, Z. Schneiderman, P. Zhang, Y. Zhu, C. Qiu, E. Kokkoli, T.-H. Wang, H.-Q. Mao, *Nat. Commun.* **2022**, *13*, 5561.
[64] S. Patel, N. Ashwanikumar, E. Robinson, Y. Xia, C. Mihai, J. P. Griffith, S. Hou, A. A. Esposito, T. Ketova, K. Welsher, J. L. Joyal, Ö. Almarsson, G. Sahay, *Nat. Commun.* **2020**, *11*, 983.
[65] L. Zheng, S. R. Bandara, Z. Tan, C. Leal, *Proc. Natl. Acad. Sci. U. S. A.* **2023**, *120*, e2301067120.
[66] M. H. Y. Cheng, J. Leung, Y. Zhang, C. Strong, G. Basha, A. Momeni, Y. Chen, E. Jan, A. Abdolahzadeh, X. Wang, J. A. Kulkarni, D. Witzigmann, P. R. Cullis, *Adv. Mater.* **2023**, *35*, 2303370.
[67] J. A. Champion, S. Mitragotri, *Proc. Natl. Acad. Sci. U. S. A.* **2006**, *103*, 4930.
[68] Z. Li, L. Sun, Y. Zhang, A. P. Dove, R. K. O'Rielly, G. Chen, *ACS Macro Lett.* **2016**, *5*, 1059.
[69] G. Sharma, D. T. Valenta, Y. Altman, S. Harvey, H. Xie, S. Mitragotri, J. W. Smith, *J. Control. Release* **2010**, *147*, 408.
[70] M. V. Baranov, M. Kumar, S. Sacanna, S. Thutupalli, G. van den Bogaart, *Front. Immunol.* **2021**, *11*, 607945.
[71] M. J. Carrasco, S. Alishetty, M.-G. Alameh, H. Said, L. Wright, M. Paige, O. Soliman, D. Weissman, T. E. Cleveland, A. Grishaev, M. D. Buschmann, *Commun. Biol.* **2021**, *4*, 1.
[72] M. Cornebise, E. Narayanan, Y. Xia, E. Acosta, L. Ci, H. Koch, J. Milton, S. Sabnis, T. Salerno, K. E. Benenato, *Adv. Funct. Mater.* **2022**, *32*, 2106727.
[73] M. Hammel, Y. Fan, A. Sarode, A. E. Byrnes, N. Zang, P. Kou, K. Nagapudi, D. Leung, C. C. Hoogenraad, T. Chen, C.-W. Yen, G. L. Hura, *ACS Nano* **2023**, *17*, 11454.
[74] P. P. G. Guimaraes, R. Zhang, R. Spektor, M. Tan, A. Chung, M. M. Billingsley, R. El-Mayta, R. S. Riley, L. Wang, J. M. Wilson, M. J. Mitchell, *J. Control. Release* **2019**, *316*, 404.
[75] R. L. Ball, K. A. Hajj, J. Vizelman, P. Bajaj, K. A. Whitehead, *Nano Lett.* **2018**, *18*, 3814.
[76] S. A. Dilliard, Q. Cheng, D. J. Siegwart, *Proc. Natl. Acad. Sci. U. S. A.* **2021**, *118*, e2109256118.
[77] X. Jiang, B. Du, J. Zheng, *Nat. Nanotechnol.* **2019**, *14*, 874.
[78] S. Guedan, H. Calderon, A. D. Posey, M. V. Maus, *Mol. Ther. – Methods Clin. Development* **2019**, *12*, 145.
[79] W. Li, S. Qiu, J. Chen, S. Jiang, W. Chen, J. Jiang, F. Wang, W. Si, Y. Shu, P. Wei, G. Fan, R. Tian, H. Wu, C. Xu, H. Wang, *Immunity* **2020**, *53*, 456.
[80] W. Li, H. Yang, L. Li, H. Wang, *J. Mol. Cell Biol.* **2020**, *12*, 745.
[81] T. Smith, A. Heger, I. Sudbery, *Genome Res.* **2017**, *27*, 491.
[82] R. Core Team, R: A Language and Environment for Statistical Computing. (R Foundation for Statistical Computing, 2022).
[83] D. Robinson, A. Hayes, S. Couch, broom: Convert Statistical Objects into Tidy Tibbles **2022**.

[84] A. Zeileis, J. C. Fisher, K. Hornik, R. Ihaka, C. D. McWhite, P. Murrell, R. Stauffer, C. O. Wilke, *J. Stat. Softw.* **2020**, *96*, 1.
[85] H. Wickham, R. François, L. Henry, K. Müller, dplyr: A Grammar of Data Manipulation **2022**.
[86] H. Wickham, forcats: Tools for Working with Categorical Variables (Factors) **2021**.
[87] E. Clarke, S. Sherrill-Mix, ggbeeswarm: Categorical Scatter (Violin Point) Plots **2017**.
[88] H. Wickham, in *ggplot2: Elegant Graphics for Data Analysis*, Springer-Verlag, New York **2016**.
[89] K. Slowikowski, ggrepel: Automatically Position Non-Overlapping Text Labels with 'ggplot2' **2021**.
[90] B. Auguie, gridExtra: Miscellaneous Functions for 'Grid' Graphics **2017**.
[91] T. L. Pedersen, patchwork: The Composer of Plots **2020**.
[92] H. Wickham, J. Bryan, *readxl: Read Excel Files* **2022**.
[93] B. Han, Rncc: To find connected components from graph built from string hamming distances **2018**.
[94] H. Wickham, stringr: Simple, Consistent Wrappers for Common String Operations **2019**.
[95] H. Wickham, M. Girlich, *tidyr: Tidy Messy Data* **2022**.
[96] E. Dolstra, https://dspace.library.uu.nl/handle/1874/7540, (accessed: July 2023).